Analyst

PAPER

View Article Online
View Journal | View Issue

Cite this: *Analyst*, 2015, **140**, 3150

Simultaneous imaging of the topography and electrochemical activity of a 2D carbon nanotube network using a dual functional L-shaped nanoprobe†

Eunjoo Lee,[a] Jungwoo Sung,[b] Taechang An,[c] Heungjoo Shin,*[d] Hong Gil Nam*[e] and Geunbae Lim*[b]

Received 21st November 2014,
Accepted 9th March 2015

DOI: 10.1039/c4an02139h

www.rsc.org/analyst

The application of nanomaterials for biosensors and fuel cells is becoming more common, but it requires an understanding of the relationship between the structure and electrochemical characteristics of the materials at the nanoscale. Herein, we report the development of scanning electrochemical microscopy–atomic force microscopy (SECM–AFM) nanoprobes for collecting spatially resolved data regarding the electrochemical activity of nanomaterials such as carbon nanotube (CNT) networks. The fabrication of the nanoprobe begins with the integration of a CNT-bundle wire into a conventional AFM probe followed by the deposition of an insulating layer and cutting of the probe end. In addition, a protrusive insulating tip is integrated at the end of the insulated CNT-bundle wire to maintain a constant distance between the nanoelectrode and the substrate; this yields an L-shaped nanoprobe. The resulting nanoprobes produced well-fitted maps of faradaic current data with less than 300 nm spatial resolution and topographical images of CNT networks owing to the small effective distance (of the order of tens of nanometers) between the electrode and the substrate. Electrochemical imaging using the L-shaped nanoprobe revealed that the electrochemical activity of the CNT network is not homogeneous and provided further understanding of the relationship between the topography and electrochemical characteristics of CNT networks.

Introduction

Nanoscale catalytic properties are still being explored in a wide range of fields. Understanding the relationship between the microstructures of nanomaterials and spatially resolved catalytic/chemical activity at the nanoscale is fundamental to the design of heterogeneous nanostructure systems.[1–5] However, the catalytic/chemical properties of nanomaterials are commonly analyzed in the bulk state and there exist technical limitations that prevent the direct mapping of the topography and catalytic activity.

Scanning electrochemical microscopy (SECM), which was developed by Bard,[6] was used to identify local redox events that occur at the ultramicroelectrode on the sample surface.[7] However, it lacks reliable tip-to-sample distance control, which limits the spatial resolution of the current plots and increases the chance of collecting the mixed information of electrochemical activity based current data and erroneous current change data caused by unstable tip-to-sample distance control. Recently, the resolution of electrochemical imaging in SECM has been improved to ~10 nm by using a nanopipette electrode; this method was applied to image nanoporous membranes.[8] However, in the electrochemical current signal, mixed information regarding the local activity and the tip-to-sample distance remains an issue.

Diverse approaches, including shear force,[9] intermittent contact (IC)–SECM,[10] combined SECM–scanning ion conductance microscopy (SICM),[11] and SECM–AFM,[12–15] have been applied to enable fine distance control of electrochemical scanning probes. Recently, double-barrel carbon nanoprobes (DBCNPs) were developed for combined SECM–SICM and were

[a]*School of Interdisciplinary Bioscience and Bioengineering, POSTECH, San31, Hyoja-dong, Nam-gu, Pohang, Gyeongsangbuk-do 790-784, Republic of Korea*
[b]*Department of Mechanical Engineering, POSTECH, San31, Hyoja-dong, Nam-gu, Pohang, Gyeongsangbuk-do 790-784, Republic of Korea*
[c]*Department of Mechanical Design Engineering, Andong National University, 1375 Gyeondong-ro, Andong, Gyeongsangbuk-do 760-749, Republic of Korea*
[d]*Department of Mechanical Engineering, UNIST, UNIST-gil 50, Ulsan, 699-798, Republic of Korea*
[e]*Center for Plant Aging Research, Institute for Basic Science, and Department of New Biology, DGIST, Daegu 711–873, Republic of Korea*
†Electronic supplementary information (ESI) available. See DOI: 10.1039/c4an02139h

used for simultaneous topographical and electrochemical imaging of a variety of substrates such as microelectrodes, nanoporous membranes, and PC12 cells.[16] In addition, scanning electrochemical cell microscopy (SECCM) with a configuration similar to the DBCNPs was used to image 2D carbon nanotube (CNT) networks and graphene electrodes.[17,18] Using the SECCM tip, the number of graphene layers and electron transfer activity were correlated by mapping the electrochemical current and optical image. In the SECCM analysis of CNT networks, the sidewalls and the closed ends of CNTs showed similar activities, which conflicts with the results of previous studies.[19] Güell[17] reported that the faradaic current at nanotube junctions was slightly higher than that at individual single-wall nanotubes (SWNTs); however, this conclusion was based on a statistical analysis of the electrochemical current images of CNTs and corresponding AFM topological images. Although this approach is innovative, its ability for the direct mapping of structures and electron transfer rates at the nanoscale is still limited.

In contrast, SECM–AFM is a versatile analytical technique that enables the visualization and quantification of local electrochemical activities as well as an analysis of the topography of the sample that is completely independent of the electrochemical current. This dual functionality is enabled by special probe geometries that ensure a fixed electrode-to-tip distance or accurate control of the tip-to-sample distance. SECM–AFM has been used to study the local electrochemical activity of various substrates, enzyme activity,[20–22] and membrane ion transport.[8,23,24] Furthermore, SECM–AFM probes with nanoelectrodes have been developed to improve the electrochemical resolution;[12,13,15,25–30] however, the application of high-resolution SECM–AFMs with disk-type nanoelectrodes is limited to the characterization of probes using the "lift-up" mode to avoid short circuiting.[27,30] In the lift-up mode, the probe tip is lifted from the substrate by a predefined distance to collect electrochemical data while tracing the surface topography recorded in the previous surface scan during which the probe was in contact with the surface. To obtain meaningful electrochemical data using SECM, the electrode should be located within several radii of the electrode from the substrate. Therefore, precise control of the tip-to-sample distance at the nanometer scale is essential for an SECM–AFM probe that features a nanoelectrode integrated at the tip apex that requires the lift-up mode. There have been some studies of special probes for SECM–AFM in order to avoid the lift-up mode and keep the distance constant between the electrode of the probe and the sample surface.[12–14,20,21,29,31] Davoodi *et al.* primarily demonstrated an L-shaped microelectrode for SECM–AFM with the lift-up mode.[32,33] The probe was integrated with a 2–5 μm diameter Pt electrode and was capable of distinguishing two active sites separated by 3–4 μm or larger.

In this study, we manufactured an L-shaped nanoprobe, which contains a protrusive peak at a disk-type tip plateau. For a high spatial electrochemical resolution, a disk-shaped CNT nanoelectrode (300 nm diameter) was integrated into the end of a commercial AFM probe tip using a sequence of processes: CNT-bundle wire synthesis, conformal insulating layer coating, and multiple focused ion-beam (FIB) milling processes. The FIB milling processes expose the disk-shaped nanoelectrode at the tip apex and pattern the insulating protrusive peak resulting in the formation of an L-shaped tip as shown in Fig. 1c. Because of its geometry, the present nanoprobe has three advantages over plain disk-type nanoprobes without the protrusive peak: first, it has a sharper tip apex than the disk-type nanoprobes, thereby ensuring relatively higher resolution topographical imaging. Second, the protrusive peak apex can prevent the electrical short problem between the electrode and conductive sample surfaces during surface scanning. Last, the nanoprobe can reduce the distance between the electrode and the sample surface to tens of nanometer, so the recycling effect enhances the electrochemical current. The L-shaped probe with a 300 nm diameter electrode facilitated simultaneous topography and electrochemical current imaging of CNT networks, thereby enabling a 300 nm spatial resolution in the imaging of the local electrochemical activity.

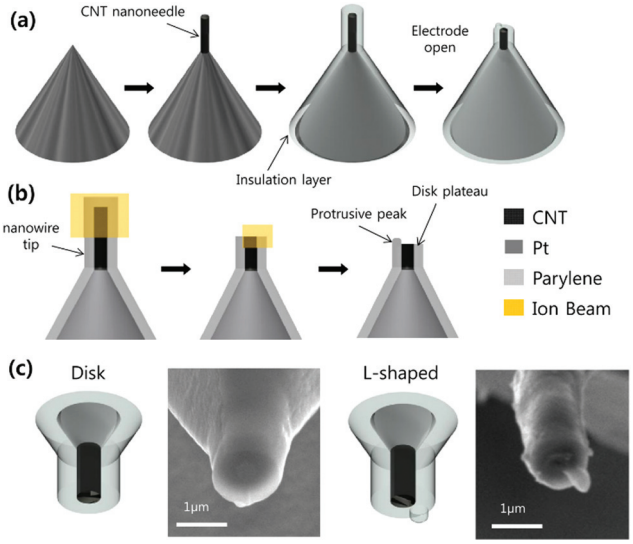

Fig. 1 Procedure for the fabrication of an L-shaped SECM–AFM nanoprobe: (a) overall scheme for the fabrication of the CNT nanoprobe, (b) FIB milling to produce the L-shaped tip end, (c) scanning electron microscopy images of a disk-type nanoprobe without a protrusive tip end and the L-shaped nanoprobe.

Experimental

Probe fabrication

The SECM–AFM nanoprobe was fabricated by integrating a CNT-bundle wire onto a conventional AFM probe (ElectriCont-G; BudgetSensors, Sofia, Bulgaria; resonance frequency = 13 kHz, force constant = 0.2 N m^{-1}, double-sided Cr/Pt coating). In this experiment, SWNTs, which were manufactured using an arc discharge process, were purchased from Hanwha

Nanotech (Incheon, Korea). A SWNT suspension was prepared by sonicating 10 mg of SWNTs in 100 mL of H_2SO_4–HNO_3 (3 : 1) for 2 h followed by centrifugation at 12 000 rpm for 10 min and two successive rinsing steps with deionized water. A CNT-bundle wire was integrated on the AFM tip apex through dielectrophoresis and surface suspension, as described in a previous study.[34] The CNT-bundle wire, which comprises a tangle of multiple SWNTs as shown in Fig. S1a and b in the ESI,† acts as an electrode in the SECM–AFM nanoprobe. During the dielectrophoresis (DEP)-based CNT-bundle wire formation process, a tight mechanical and electric contact is formed between the CNTs and the metal surface of the AFM probe without an additional bonding process. The diameter of the CNT-bundle wire is scalable from 50 nm to 1 μm by controlling the DEP processing conditions such as electric potential frequency and amplitude. In this study, CNT bundle wires with 300–400 nm diameters were integrated into SECM–AFM nanoprobes (Fig. S1c†).

After integrating the CNT bundle wire onto the tip apex, the AFM probe was electrically connected to an electrical signal line using silver epoxy. Then the AFM probe connected with the signal line was cured at 110 °C for 50 min. Then, a 300–400 nm thick parylene-C (Dichlorodi-p-xylylene, Daisan Kasei Co., Tokyo, Japan) insulation layer was deposited on the AFM probe (Parylene coater; Alphaplus Co., Pohang, South Korea). Finally, the tip geometry of the L-shaped nanoprobe was defined by cutting the parylene-C-coated CNT-bundle wire *via* FIB milling (Quanta 3D FEG, FEI company, USA); this process also exposed a disk-shaped CNT nanoelectrode (Fig. 1c). The ion-beam current was limited to <50 pA to avoid the formation of debris at the cutting area that would hinder clear exposure of the CNT electrode. The protrusive peaks of the L-shaped nanoprobes had a diameter of 300–400 nm and a height of 300–400 nm.

CNT network

A pair of microsized 1000/100 Å thick gold/chrome band electrodes separated by a 50 μm gap was patterned using a lift-off process. The SWNT suspension (*i.e.*, the same solution used for the formation of the CNT-bundle wire) was then dropped between the two parallel gold electrodes and an AC potential of 1 MHz, 1 V_{p-p}, was applied to the electrodes thereby forming a randomly distributed CNT network by DEP force. The DEP force primarily forced metallic CNT or metallic CNT bundles to assemble between the pair of electrodes instead of semiconducting CNTs.[35] Finally, the remaining CNT suspension droplets were removed to leave a CNT network between the electrodes. These CNT-gold electrodes were used as counter electrodes in the electrochemical experiments using the L-shaped SECM–AFM probes. The large surface area of the gold electrodes enables fast electron flow during a half-cell reaction.

SECM–AFM system set-up

A conventional AFM instrument (SPA 400; Seiko, Tokyo, Japan) installed inside a shielded cage was used for the SECM–AFM measurements. All electrochemical measurements were performed using a Modulab potentiostat (Solartron Analytical, Farnborough, Hampshire, U.K.). The faradaic current signal from the potentiostat was converted into a voltage signal and then transmitted to the AFM machine for synchronized dual imaging of the surface topography and electrochemical activity of the sample surface. The electrochemical data were measured using a three-electrode cell system comprising a CNT-gold electrode as the counter electrode, a platinum wire as the reference electrode, and an AFM cantilever as the working electrode. All electrochemical experiments were performed in 20 mM $K_3Fe(CN)_6$ solution with 0.5 M KCl.

Results and discussion

The electrochemical behavior of the CNT nanoelectrodes and the parylene-C insulating layer quality were characterized using cyclic voltammetry in 20 mM $K_3Fe(CN)_6$ with 0.5 M KCl electrolyte solution, as shown in Fig. 2. No significant redox peak was observed in the cyclic voltammogram from the nanoprobe of which the electrode was not exposed using FIB. This result confirms that the nanoprobe was well-insulated by the parylene-C layer (inset image of Fig. 2). After FIB processing, the nanoprobe electrode showed clear reduction and oxidation peaks in the cyclic voltammogram. For disk-shaped electrodes, the diffusion-limited current is described as:

$$i_\infty = 4nFcDr \quad (1)$$

where n is the number of electrons transferred per reaction, F is the Faraday constant, r is the radius of the electrode, D is the diffusion coefficient, and c is the bulk concentration of the electroactive species.[30] The diameter of the electrode of the L-shaped nanoprobe was approximately 300 nm (Fig. 1c); therefore, the expected diffusion-limited current is about 1 nA.

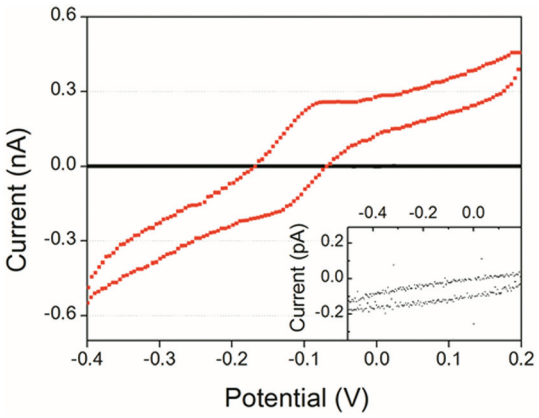

Fig. 2 Cyclic voltammograms from an L-shaped nanoprobe before (black squares in the inset graph) and after FIB cutting (red squares). The voltammograms of the nanoprobes show redox peaks after FIB cutting in 20 mM $K_3Fe(CN)_6$ and 0.5 M KCl solution. The scan rate was 50 mV s^{-1}.

Fig. 2 shows that the diffusion-limited current of the L-shaped nanoprobes is about 450 pA, which is approximately half of the theoretically expected current. It is inferred that this disagreement originates from a difference between the effective electrode area and the structural electrode area. Even with tight control of the FIB milling process, the formation of some parylene-C debris is inevitable.[28] Moreover, the CNT wires are not always as perfectly packed as shown in the TEM image in Fig. S1b;† therefore, the effective electrode area can be smaller than the overall CNT-bundle wire size. The other potential cause of the unexpectedly low diffusion-limited current is the close proximity of the protrusive parylene-C peak to the electrode, which hinders the diffusion of the redox species to the electrode.

Randomly distributed 2D CNT networks are widely used for protein sensors, gas sensors, fuel-cell devices, and fundamental studies on the characterization of CNTs.[36] In this study, a CNT network was constructed on a SiO_2-coated silicon wafer using dielectrophoresis. The CNT network consists of CNT bundles that range between 100 and 300 nm wide and 50–60 nm high, as determined *via* FESEM (Fig. 3b) and AFM (not shown here). In the SECM–AFM experiment, the network of CNTs, which was connected to gold band electrodes (Fig. 3a), was imaged to concurrently map the topographical and electrochemical current (EC) images using the L-shaped nanoprobe.

Using the L-shaped nanoprobe, topographical and EC images of CNT networks in 20 mM $K_3Fe(CN)_6$ and 0.5 M KCl electrolyte were simultaneously collected using the AFM contact mode. The small distance between the electrode and the surface, which is determined by the protrusive peak height, ensures high spatial resolution for electrochemical imaging as well as stable electrochemical data collection during a single surface scan; this reduces the total scanning time by half compared to the "lift-up" mode. Topographical and EC images of 8 μm × 8 μm areas of the CNT network were successfully collected without any short circuiting problem even in the contact mode because of the fixed distance between the protrusive peak and the electrode surface of the L-shaped nanoprobe. In the EC image, the output current signal, which was obtained using a potentiostat, was an analog signal with electrical noise primarily at 60 Hz. These sinusoidal noises were successfully filtered using a fast Fourier-transform filter.

In topographical imaging, spatial resolution mainly depends on the size of the protrusive peak. The topographical images of the CNT network obtained from the L-shaped probe reveal that the CNT wire width ranges from 170 to 500 nm; these values are greater than those obtained using a conventional AFM probe. This disagreement is caused by the probe convolution effect, which is a result of the relatively large tip radius.

In the topographical images of the CNT network (Fig. 3c) obtained using the L-shaped nanoprobe, two duplicate profiles from a single CNT wire are repeated along a line that is tilted in a specific direction (Fig. S2d†). The duplicate topographical profiles originate from the presence of two contacts between the nanoprobe tip and substrate owing to the small vertical spacing between the protrusive peak and the edge of the disk plateau, which is denoted by Z_{shift} in Fig. 4a As the contact-mode scanning proceeds, an additional contact with the substrate at the edge of the disk plateau occurs subsequent to the first contact between the protrusive peak and the substrate. These two successive contacts induce an ~700 nm shift on the *XY* plane and a 15 nm shift in the *z*-direction in the second topographical profile. This effect can be more clearly demonstrated in a frequency domain: black line patterns repeated in parallel were observed in the frequency response of the topographical image from the L-shaped nanoprobes (Fig. S2d and S3c†). Generally, images with noise from 1D motion show repeated parallel lines in the frequency response, and the direction of motion is the same as that of a line perpendicular to the repeated parallel lines.[35] In this case, the repeated lines of the frequency response were tilted 54° from the AFM scan direction; this direction coincides with the relative position of the edge of the disk plateau that produces the second profile from the protrusive peak. No repeated pattern was evident in the frequency response of the current image (Fig. S2e†), which corresponds well with the single profile of the current image shown in Fig. 3d.

During scanning, a −0.1 V bias was applied to the nanoprobe electrode *versus* the platinum wire reference electrode. The distance between the nanoelectrode and the sample surface, d_{eff}, is maintained as the probe tip scans along the flat sample surface and climbs the CNT sidewall. However, d_{eff} is reduced once the protrusive peak steps down from the CNT and the second contact between the edge of the disk plateau and the CNT occurs, as delineated in Fig. 4a. These two dis-

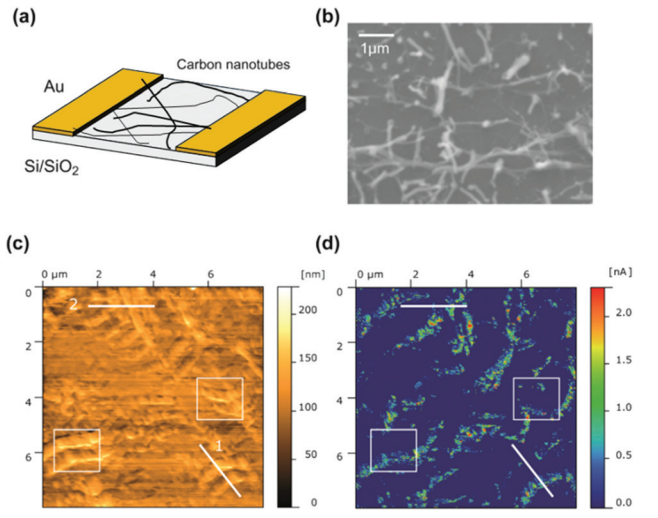

Fig. 3 (a) A schematic diagram and (b) an FESEM image of a CNT network with a gold electrode. (c) A topographical image and (d) an electrochemical current image of an 8 μm × 8 μm area of the CNT network measured using an L-shaped nanoprobe at −0.1 V *vs.* a Pt reference electrode with a scan rate of 0.5 Hz.

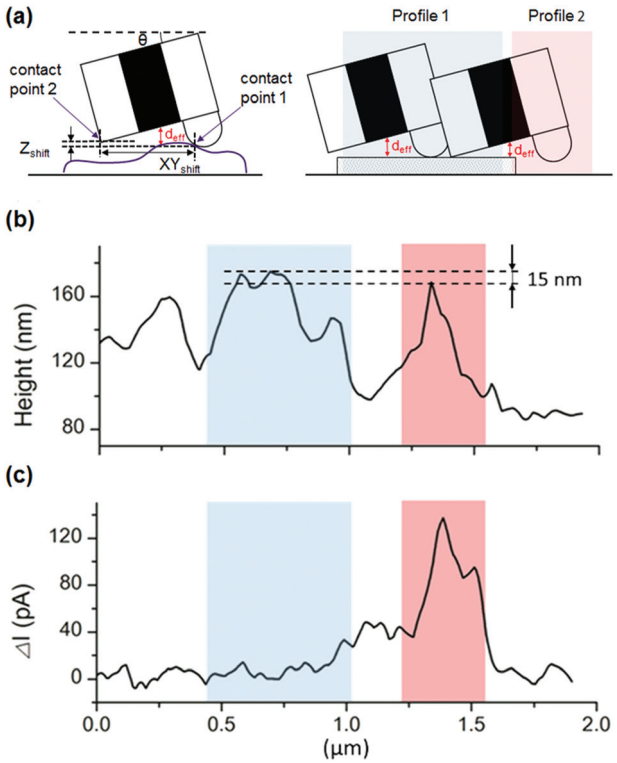

Fig. 4 (a) Schematic diagrams of surface scanning using the L-shaped nanoprobe, cross-sectional profiles of (b) the topographical and (c) the reduction current images of a CNT wire along line 1 in Fig. 3 (blue box: 1st profile, red box: 2nd profile).

crete electrode-to-sample-surface distances can be used to explain the single CNT profile in the EC image. In the AFM topographical image, the peak height of the second profile of the CNTs is 15 nm lower than that of the first profile (Fig. 4b), which indicates a shorter d_{eff} in the second profile. Between the proximate nanoelectrode and conductive CNT surface, the reduced species, *i.e.*, $[Fe(CN)_6]^{4-}$, generated at the probe electrode diffuse to the CNT surface and become oxidized; the oxidized species then diffuse back to the electrode surface. This recycling reaction is called the positive feedback effect and occurs more efficiently as the electrode to surface distance decreases. Accordingly, the redox current increased in the second profile of the CNT because of the enhanced positive feedback effect due to reduced diffusion distance (Fig. 4c). The current signal level of the second profile of the CNT network was in the hundreds of picoamperes range while the current level of the first profile was too low to be distinguished from the background current; these results are shown in the two boxes of Fig. 3c and d. In the electrochemical current image (Fig. 3d), only a single strand-type CNT profile is evident, whereas duplicate strand-type CNT profiles occur in the topographic image. The CNT widths in the EC image are similar to or slightly smaller than the CNT sizes shown *via* topography; this indicates that the positive feedback effect is enhanced significantly only when the nanoelectrode is located very close to the CNT surface.

Moreover, step-like gold electrodes were imaged to quantify the spatial resolutions of the topographical and electrochemical current (EC) images, as shown in ESI Fig. S4.† [37] The EC spatial resolution was as high as the topological resolution (~300 nm).

CNTs are known to be electrochemically active at the end sites and less active at the sidewalls of the nanotubes in bulk experiments.[19] However, recent experimental results using a nanopipette electrochemical cell revealed that both the sidewalls and ends of CNTs exhibited a fast electrochemical electron transfer rate.[19] In the electrochemical current image of the CNT network measured using the L-shaped probe (Fig. 3d and 5b), the electrochemical current was amplified when the distance between the nanoelectrode and CNT surface was minimized at the second contact. The current signal increment is due to the redox cycling effect when the electrode-to-sample distance becomes very small. Almost all the CNT components, including the junctions and individual CNT wires, show active and heterogeneous electrochemical behaviors at both the longitudinal sidewalls and end sites.

It is inferred that the local heterogeneity of the electrochemical characteristics of CNTs is caused by either local or overall defects on the nanotubes because of the fluctuations in the synthetic conditions, contamination by impurities, or heterogeneous composition, *i.e.*, including both semiconducting and metallic CNTs. CNTs are typically classified as either semiconducting or metallic nanotubes depending on their electron transfer rates, which are based on the structure and the arrangement of the angles of the carbon sheet. CNT networks constructed using DEP mainly comprise metallic CNTs; however, some semiconducting CNTs can be present in the CNT network owing to imperfect DEP-based filtration. In addition, it has been reported that even small mechanical perturbations (*e.g.*, bent or kinked CNTs) can change the electrical conductivity of the CNT from metallic to semiconducting owing to electrostatic gating.[38] The electrical bias on the nanoelectrode of the L-shaped probe tip during the electrochemical current measurement could induce local gating on the metallic CNTs resulting in the heterogeneous electrochemical activity of the CNTs. The electrochemical current signal distri-

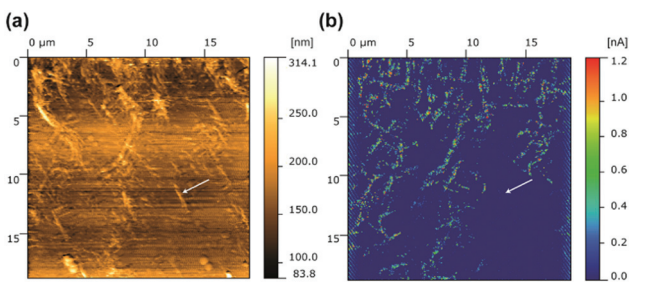

Fig. 5 (a) A topographical image and (b) an EC image of a 19 μm × 19 μm area of a CNT network at −0.1 V *vs.* a Pt reference electrode with a 0.5 Hz scan rate.

bution is also influenced by the electrical conductivity through the CNT junctions. It has been reported that the junctions and alignment of the CNT network significantly influence the electrical conductivity of electronic nanodevices based on CNTs.[3,38] In Fig. 5 the right bottom area of the CNT network does not show a significant reduction current signal. This phenomenon is clearly evident at the CNT segments that are indicated with arrows in Fig. 5. On the upper portion of the CNT network in Fig. 5, the CNTs are connected to a micrometer-sized gold counter electrode towards which electrons from the oxidation events at the CNT surfaces flow. Therefore, the segments and parts of the CNT network that are not electrically connected to the gold electrode show little or no electrochemical activity because the isolated CNT network is as small as the CNT nanoprobe and bipolar behavior in the CNT network is not significant.[39]

Conclusion

In summary, a novel L-shaped SECM–AFM nanoprobe was fabricated to collect the spatially resolved electrochemical activity data and corresponding topography of nanomaterials. The nanoprobe was integrated with a CNT nanoelectrode and a protrusive peak that maintains a short distance between the electrode and substrate, thereby enhancing the redox current and avoiding short-circuit problems. A single surface scan measurement achieved simultaneous topography imaging and electrochemical current mapping of a CNT network with a spatial resolution of 300 nm for the electrochemical activity. Mapping of the topography and EC image of the CNT networks revealed heterogeneous redox reactions occurring on the overall CNT network including the single wires and CNT junction points.

The small protrusive peak and the disk plateau of the L-shaped nanoprobe caused duplicate profiles of the CNTs; this interference can be reduced by trimming the edge of the disk plateau where the second contact occurs. In addition, the spatial resolution of the topographical image is expected to improve by sharpening the protrusive peak apex through additional FIB milling processes. Despite some limitations of the L-shaped nanoprobe, SECM–AFM scanning using the nanoprobe achieved successful visualization and mapping of the structure and the local electrochemical activity of the nanocomposite samples; this provided data on the electrochemical characteristics of the nanomaterials at the nanoscale and the effect of the network structure on the local electrochemical activity of nanomaterials.

Acknowledgements

This work was supported by the National Research Foundation of Korea (NRF) grant funded by the Korea government (MSIP) (NRF-2012R1A2A2A06047424), the National Honor Scientist Support Program (no. 20100020417), the Institute for Basic Science (IBS-R013-D1-2014-a00), and the Basic Science Research Program (NRF-2013R1A1A2009711).

Notes and references

1 B. R. Azamian, J. J. Davis, K. S. Coleman, C. B. Bagshaw and M. L. H. Green, *J. Am. Chem. Soc.*, 2002, **124**, 12664–12665.
2 W. Zhang, W. Jin, T. Fukushima, A. Saeki, S. Seki and T. Aida, *Science*, 2011, **334**, 340–343.
3 B. Y. Lee, M. G. Sung, H. Lee, S. Namgung, S. Y. Park, D. S. Choi and S. Hong, *NPG Asia Mater.*, 2010, **2**, 103–111.
4 C. K. Chan, H. Peng, G. Liu, K. McIlwrath, X. F. Zhang, R. A. Huggins and Y. Cui, *Nat. Nanotechnol.*, 2008, **3**, 31–35.
5 H. Zhang, G. Cao and Y. Yang, *Energy Environ. Sci.*, 2009, **2**, 932–943.
6 A. J. Bard, F. R. F. Fan, J. Kwak and O. Lev, *Anal. Chem.*, 1989, **61**, 132–138.
7 G. Wittstock, M. Burchardt, S. E. Pust, Y. Shen and C. Zhao, *Angew. Chem., Int. Ed.*, 2007, **46**, 1584–1617.
8 M. Shen, R. Ishimatsu, J. Kim and S. Amemiya, *J. Am. Chem. Soc.*, 2012, **134**, 9856–9859.
9 A. Hengstenberg, C. Kranz and W. Schuhmann, *Chem. – Eur. J.*, 2000, **6**, 1547–1554.
10 K. McKelvey, M. A. Edwards and P. R. Unwin, *Anal. Chem.*, 2010, **82**, 6334–6337.
11 Y. Takahashi, A. I. Shevchuk, P. Novak, Y. Murakami, H. Shiku, Y. E. Korchev and T. Matsue, *J. Am. Chem. Soc.*, 2010, **132**, 10118–10126.
12 J. V. Macpherson and P. R. Unwin, *Anal. Chem.*, 2000, **72**, 276–285.
13 C. Kranz, G. Friedbacher, B. Mizaikoff, A. Lugstein, J. Smoliner and E. Bertagnolli, *Anal. Chem.*, 2001, **73**, 2491–2500.
14 J. Wiedemair, B. Balu, J.-S. Moon, D. W. Hess, B. Mizaikoff and C. Kranz, *Anal. Chem.*, 2008, **80**, 5260–5265.
15 P. S. Dobson, J. M. R. Weaver, M. N. Holder, P. R. Unwin and J. V. Macpherson, *Anal. Chem.*, 2005, **77**, 424–434.
16 Y. Takahashi, A. I. Shevchuk, P. Novak, Y. Zhang, N. Ebejer, J. V. Macpherson, P. R. Unwin, A. J. Pollard, D. Roy, C. A. Clifford, H. Shiku, T. Matsue, D. Klenerman and Y. E. Korchev, *Angew. Chem., Int. Ed.*, 2011, **50**, 9638–9642.
17 A. G. Güell, N. Ebejer, M. E. Snowden, K. McKelvey, J. V. Macpherson and P. R. Unwin, *Proc. Natl. Acad. Sci. U. S. A.*, 2012, **109**, 11487–11492.
18 A. G. Güell, N. Ebejer, M. E. Snowden, J. V. Macpherson and P. R. Unwin, *J. Am. Chem. Soc.*, 2012, **134**, 7258–7261.
19 J. J. Gooding, *Electrochim. Acta*, 2005, **50**, 3049–3060.
20 A. Kueng, C. Kranz, A. Lugstein, E. Bertagnolli and B. Mizaikoff, *Angew. Chem., Int. Ed.*, 2003, **42**, 3238–3240.
21 C. Kranz, A. Kueng, A. Lugstein, E. Bertagnolli and B. Mizaikoff, *Ultramicroscopy*, 2004, **100**, 127–134.
22 A. Anne, A. Chovin, C. Demaille and M. Lafouresse, *Anal. Chem.*, 2011, **83**, 7924–7932.

23 C. E. Gardner, P. R. Unwin and J. V. Macpherson, *Electrochem. Commun.*, 2005, **7**, 612–618.
24 A. Kueng, C. Kranz, A. Lugstein, E. Bertagnolli and B. Mizaikoff, *Angew. Chem., Int. Ed.*, 2005, **44**, 3419–3422.
25 Y. Hirata, S. Yabuki and F. Mizutani, *Bioelectrochemistry*, 2004, **63**, 217–224.
26 J. Abbou, C. Demaille, M. Druet and J. Moiroux, *Anal. Chem.*, 2002, **74**, 6355–6363.
27 D. P. Burt, N. R. Wilson, J. M. R. Weaver, P. S. Dobson and J. V. Macpherson, *Nano Lett.*, 2005, **5**, 639–643.
28 P. S. Dobson, J. M. R. Weaver, D. P. Burt, M. N. Holder, N. R. Wilson, P. R. Unwin and J. V. Macpherson, *Phys. Chem. Chem. Phys.*, 2006, **8**, 3909–3914.
29 H. Shin, P. J. Hesketh, B. Mizaikoff and C. Kranz, *Sens. Actuators, B*, 2008, **134**, 488–495.
30 A. J. Wain, D. Cox, S. Zhou and A. Turnbull, *Electrochem. Commun.*, 2011, **13**, 78–81.
31 S. E. Pust, M. Salomo, E. Oesterschulze and G. Wittstock, *Nanotechnology*, 2010, **21**, 105709.
32 A. Davoodi, A. Farzadi, J. Pan, C. Leygraf and Y. Zhu, *J. Electrochem. Soc.*, 2008, **155**, C474–C485.
33 A. Davoodi, J. Pan, C. Leygraf and S. Norgren, *Electrochim. Acta*, 2007, **52**, 7697–7705.
34 T. An, W. Choi, E. Lee, I. Kim, W. Moon and G. Lim, *Nanoscale Res. Lett.*, 2011, **6**, 306.
35 R. Krupke, F. Hennrich, H. B. Weber, M. M. Kappes and H. v. Löhneysen, *Nano Lett.*, 2003, **3**, 1019–1023.
36 T. An, K. S. Kim, S. K. Hahn and G. Lim, *Lab Chip*, 2010, **10**, 2052–2056.
37 G. Wittstock, H. Emons, T. H. Ridgway, E. A. Blubaugh and W. R. Heineman, *Anal. Chim. Acta*, 1994, **298**, 285–302.
38 H. Jeong, H. M. Gweon, B. J. Kwon, Y. H. Ahn, S. Lee and J.-Y. Park, *Nanotechnology*, 2009, **20**, 345202.
39 A. I. Oleinick, D. Battistel, S. Daniele, I. Svir and C. Amatore, *Anal. Chem.*, 2011, **83**, 4887–4893.